

Electronic Supplementary Information

**Ground-state charge-transfer interactions in
donor:acceptor pairs of organic semiconductors.**

**A spectroscopic study of two representative
systems**

Giuliano Duva,^{*,†} Paul Beyer,^{‡,||} Reinhard Scholz,[¶] Valentina Belova,^{†,⊥} Andreas
Opitz,[‡] Alexander Hinderhofer,^{*,†} Alexander Gerlach,[†] and Frank Schreiber^{†,§}

[†]*University of Tübingen, Institute for Applied Physics, Auf der Morgenstelle 10, 72076
Tübingen, Germany*

[‡]*Humboldt-Universität zu Berlin, Department of Physics, Newtonstraße 15, 12489 Berlin,
Germany*

[¶]*Dresden Integrated Center for Applied Physics and Photonic Materials, Nöthnitzer Str.
61, 01187 Dresden, Germany*

[§]*Center for Light-Matter Interactions, Sensors & Analytics (LISA⁺), Auf der Morgenstelle
15, 72076 Tübingen, Germany*

^{||}Present address: ESRF The European Synchrotron, 71, Avenue des Martyrs, 38000
Grenoble, France.

[⊥]Present address: ICMAB-CSIC, Campus de la UAB, E-08191 Bellaterra, Spain.

E-mail: giuliano.duva@uni-tuebingen.de; alexander.hinderhofer@uni-tuebingen.de

Preparation and characterization of SiO_x thin films on Au substrates *via* plasma-enhanced chemical vapor deposition (PECVD)

Si wafers coated with 5 nm Ti adhesion layer and 200 nm Au ($\sim 10 \times 15 \text{ mm}^2$) were used as substrates for the deposition of the SiO_x . The Au substrates were cleaned first with acetone and then with isopropanol in an ultrasonic bath and subsequently dried under a gentle stream of N_2 . The Au slides were then transferred into a Plasmalab 800Plus (Oxford Instruments), heated to 300°C and kept at this temperature during the deposition of the SiO_x film. We used a plasma power of 30 W and a gas mixture of 16% SiH_4 and 25% N_2O in a N_2 carrier gas flow. The total pressure in the reaction chamber was 1 Torr. Since the thickness of the oxide layer can be controlled by the deposition time, we tested several. We then characterized the produced layers using atomic force microscopy (AFM), optical microscopy and ellipsometry. The results obtained for the SiO_x film thickness as function of the deposition time are summarized in Tab. S1.

Table S1: Summary of the estimated thicknesses for the SiO_x layers deposited on the Au substrates.

test substrate	1	2	3	4	5
plasma power (W)	30	30	30	15	15
deposition time (s)	5	8	12	15	24
oxide thickness (nm)	8	12	18	18	27

For the production of our organic thin films we chose the substrates having an oxide thickness of 12 nm, which we found to be the best compromise between thickness and layer homogeneity. An oxide thickness of 12 nm assures high reflectivity of the substrate and conservation of the surface selection rules³ and at the same time efficiently decouples the organic layer from the metal surface.

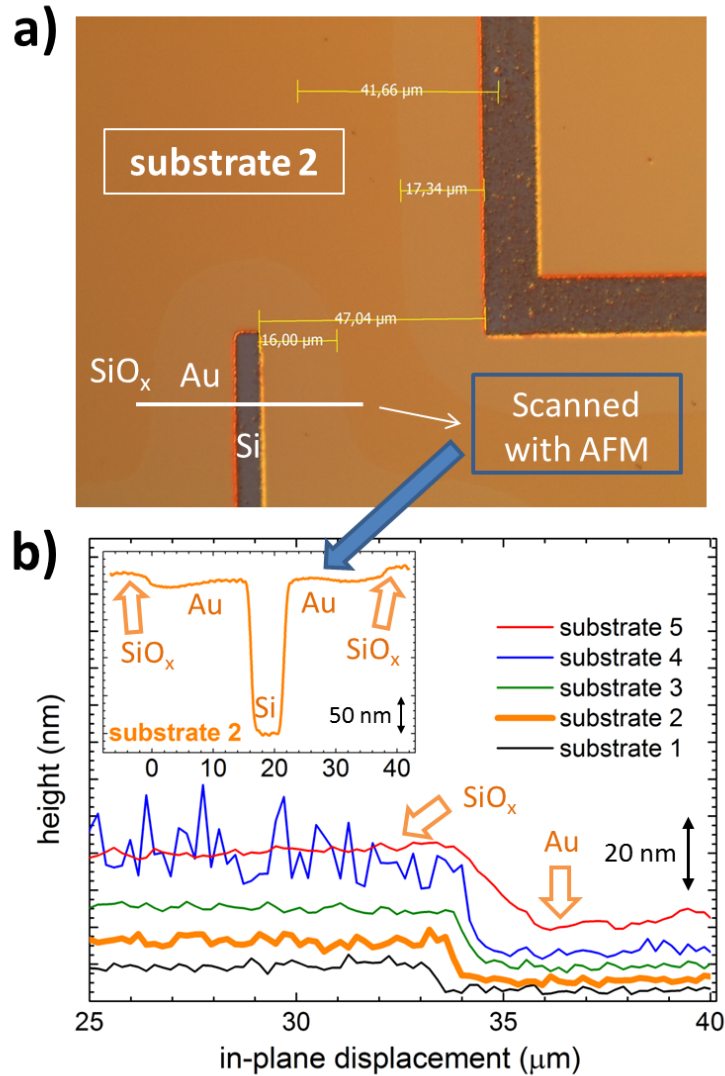


Figure S1: a) Optical microscope image of the test substrate 2 (plasma power: 30 W, deposition time: 8 s, estimated Si oxide thickness: 12 nm). The dark-brown areas were selectively etched using a mask in order to reach the layer below the Au coating. These dark areas are surrounded by a light-orange contour roughly 17 μm wide, which shows the exposed Au surface after selective etch of the SiO_x coating. The remaining dark-orange areas show the oxide coating, which remarkably can be recognized already under the optical microscope thanks to its contrast with the underlying Au substrate. The white-highlighted line was further scanned under the AFM, as shown in the inset below. a) AFM scans of test substrates 1-5, where the SiO_x layer has been removed in order to show the SiO_x-to-Au step (orange arrow). All AFM scans were analyzed using the software Gwiddion¹. Clearly the oxide thickness increases with deposition time and plasma power, as shown in Tab. S1. Notice that for substrate 4 the deposition parameters do not allow a homogeneous coverage of the oxide surface. The inset shows a line scan along the surface of the test substrate 2 including the SiO_x-to-Au step and the etched Au channel.

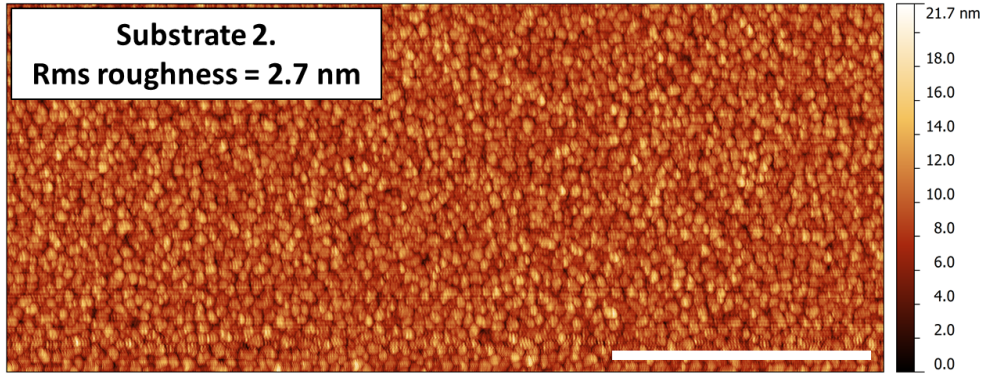


Figure S2: AFM scan of the test substrate 2 (plasma power: 30 W, deposition time: 8 s, estimated Si oxide thickness: 12 nm). The roughness calculated on this image is reported in the top left corner. The inset scale bar corresponds to 2 μm . As it can be seen, the surface is homogeneously covered by the Si oxide.

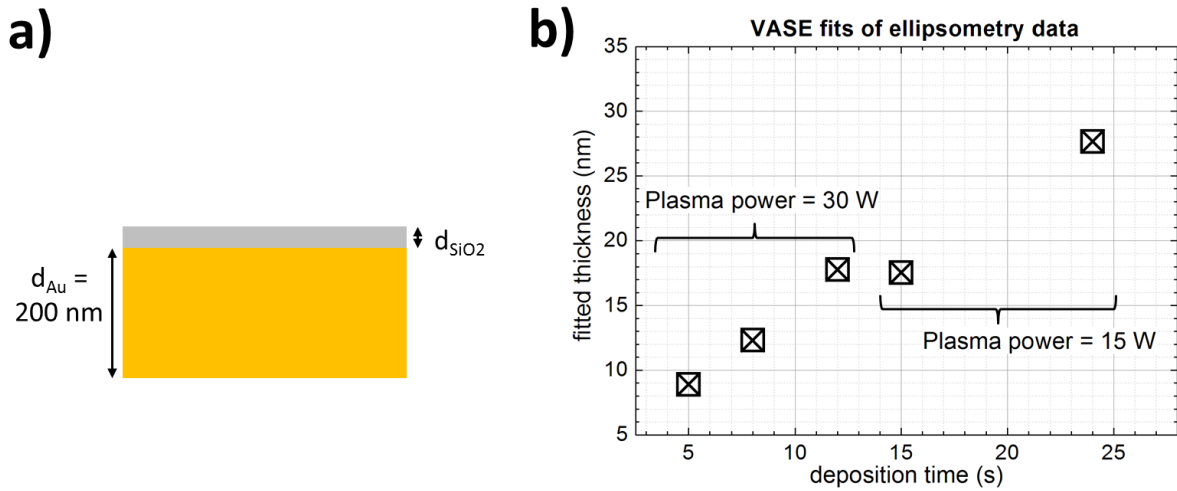


Figure S3: (a) Optical model employed in the VASE² software for fitting the ellipsometry data on the test SiO_x/Au substrates. The model simply consists of a Si dioxide layer on top of a 200 nm-thick Au substrate. For simplicity no roughness of the Au/SiO_x and SiO_x/air interfaces is included, which nevertheless produces very good fits. (b) Thickness values obtained from the fits. The thickness values match very well the AFM scans shown in Fig. S1.

AFM data

Here we show AFM data measured for the DIP:F₆TCNNQ mixtures studied in this work.

AFM height-profiles

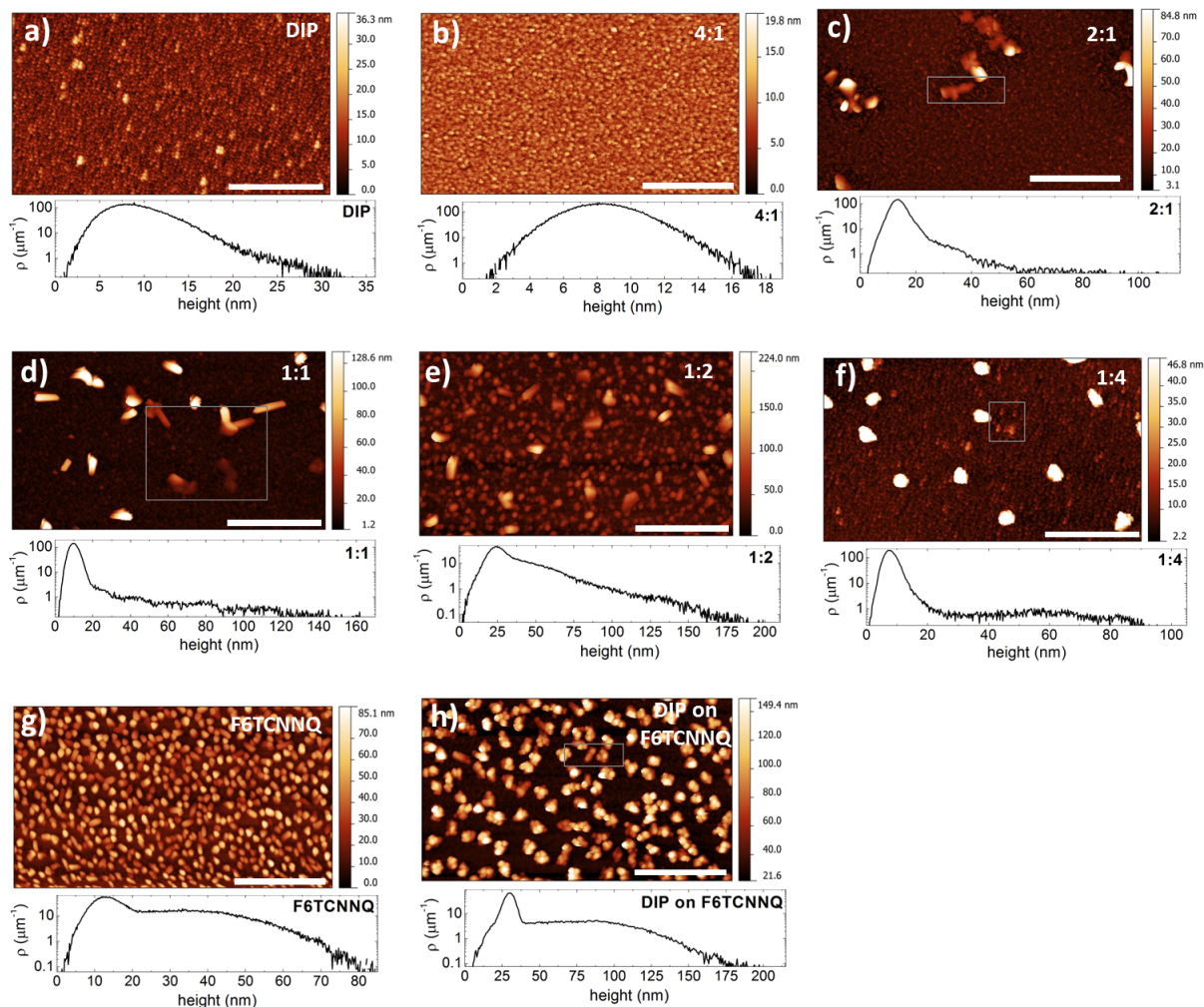


Figure S4: $4 \times 7 \mu\text{m}^2$ AFM scans of DIP:F₆TCNNQ blends in varying mixing ratios grown on SiO_x/Au substrates. For the scans of the samples 2:1, 1:1, 1:4 and “DIP on F₆TCNNQ”, the extremes of the color scale were set on the area delimited by the rectangles. The inset bar corresponds to 2 μm . Height distributions are reported below the corresponding image. The root-mean square roughness of the images are: 3.4 nm (DIP), 2.0 nm (4:1), 8.8 nm (2:1), 18.2 nm (1:1), 23.4 nm (1:2), 10.6 nm (1:4), 15 nm (F₆TCNNQ), 33.1 nm (DIP on F₆TCNNQ).

The evolution of film structure as function of D:A mixing ratio has relevant consequences on film morphology. In order to illustrate this, we show in Fig. S4 AFM topographic scans and corresponding height distributions of the same films presented in Fig. 2 of the manuscript.

The morphology of the pristine DIP film exhibits small grains with some taller islands. This morphology is clearly inherited from the finely granulated SiO_x surface covering the Au substrate (Fig. S2) and is very different from that of DIP grown on native Si oxide⁴. The 4:1 blend also exhibits small grains, but their size is slightly larger than for pristine DIP and their height is more uniformly distributed.

The morphology of the blends from 2:1 to 1:4 consists of a relatively smooth background on which taller islands are present. The height distributions reported for each scan give qualitative information about the average island height. The island density increases from the 2:1 to the 1:2 blend. For the latter, islands of intermediate height are also present. For the 1:4 blend the number of taller islands decreases again. Combining the morphological information with the X-ray scattering data (see Fig. 2c-f of the manuscript) we conclude that the taller islands in the mixtures from the 2:1 up to the 1:2 constitute crystalline domains where mainly D:A co-crystals have nucleated. This conclusion is supported by the elongated shape of the taller islands in these mixtures. The islands in the 1:4 mixture, in turn, are rather isotropic and most probably constituted of segregated F_6TCNNQ due to its molar excess in this film. However, since the X-ray diffraction pattern in Fig. 2f of the manuscript shows strong features from the D:A co-crystal for this mixture, such D:A crystalline domains must be numerous and might decorate the F_6TCNNQ islands in the 1:4 mixture. The images acquired by the lock-in phase channel of the AFM for the bulk mixtures and for DIP on F_6TCNNQ (Fig. S5) corroborate the above analysis.

The pristine F_6TCNNQ film (Fig. S4g) exhibits a completely de-wetted morphology of in-plane isotropic islands, similarly to the sample with DIP on F_6TCNNQ (Fig. S4h). For the latter, by comparison with the X-ray scattering data it seems likely that rather randomly oriented DIP crystals decorate the F_6TCNNQ islands. The surface roughness between the

islands for the sample with DIP on F₆TCNNQ matches that of the bare SiO_x substrate (Fig. S2), therefore we assume that DIP crystallites preferentially nucleate on the body of the F₆TCNNQ islands leaving the inter-island space free. This morphology demonstrates that isolated, extended domains of F₆TCNNQ have been “capped” by a DIP matrix, at the same time assuring a minimized number of D:A interfaces between the two materials.

The root-mean square roughness values indicated in caption of Fig. S4 are in agreement with the qualitative analysis of the morphology. The roughness is minimal for the 4:1 mixture, which can be explained by a smoothing effect of F₆TCNNQ on the excess DIP. The roughness then increases steadily for the blends with increasing relative amount of F₆TCNNQ until the 1:4 molar ratio is reached, for which the roughness decreases. One can explain this by a smoothing effect of DIP on the excess F₆TCNNQ, analogous to the reverse effect in the 4:1 mixture. This trend of roughness as function of mixing ratio matches our observations for this system on native Si oxide⁵.

Phase-contrast AFM scans

For the AFM scans of the different DIP:F₆TCNNQ blends presented in Fig. S4, the lock-in phase signal was also recorded as shown in Fig. S5.

Phase-contrast imaging is very sensitive to the frictional properties and can therefore be used to resolve single domains based, for instance, on their degree of crystallinity or on their composition. From Fig. S5 we see that the domains exhibiting phase-contrast have a nearly 1:1 correspondence with the islands visible in the topographic images of Fig. S4. For the mixtures from 2:1 to 1:4 there is an additional peculiar intra-island contrast originating from the different surface properties of the exposed crystal facets, supporting the conclusion that the elongated islands are constituted of DIP:F₆TCNNQ co-crystals. For the 1:4 mixture the islands exhibit an isotropic shape, but the dark-bright intra-island contrast is still visible, supporting the hypothesis made in the manuscript that these islands might have an F₆TCNNQ core but they are decorated by co-crystallites.

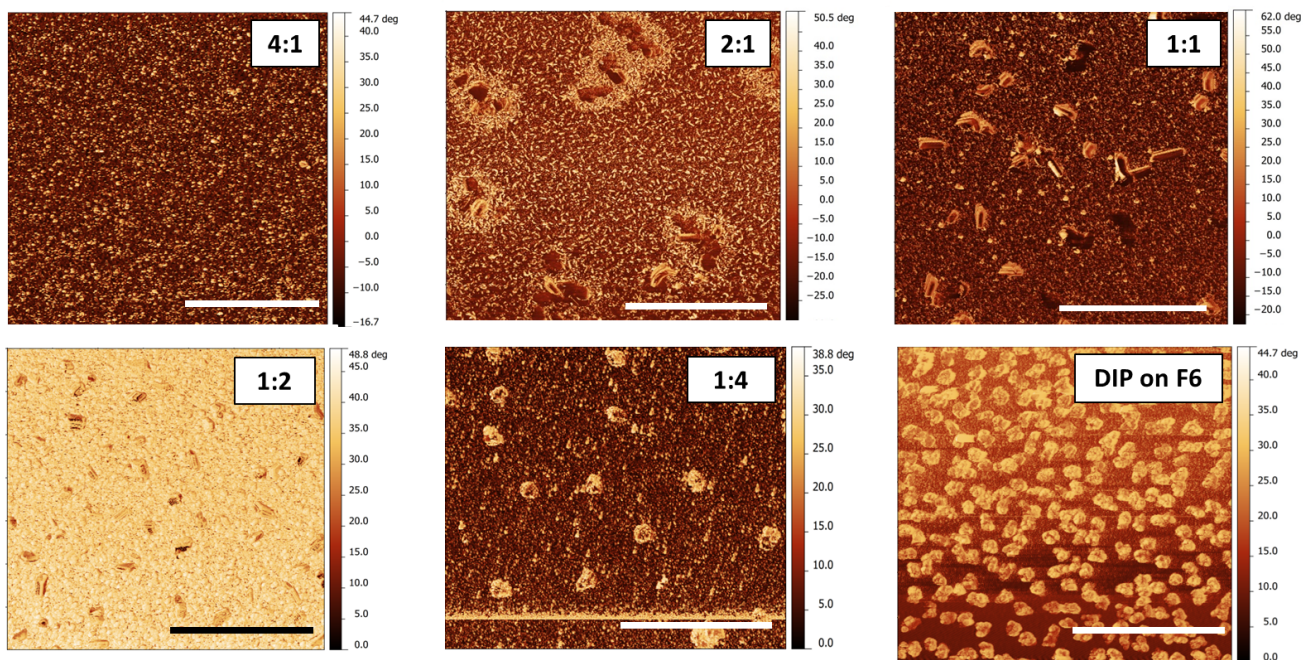


Figure S5: Lock-in phase channel recorded for the AFM scans of the different DIP:F₆TCNNQ mixed films. The inset bar corresponds to 3 μm .

Notice for the 2:1 mixture the remarkable contrast between the segregated islands of D:A co-crystallites (dark) and the surrounding DIP-rich domains with small needle-like grains (bright), which are themselves surrounded by a homogeneous matrix where the phase-separation between DIP and F₆TCNNQ on a length scale of few tens of nm is evident. This phase-contrast scan illustrates the possibly very complicated scenarios of co-crystal formation *vs* phase separation for the material system DIP:F₆TCNNQ⁶.

Setup for PMIRRAS

The typical setup for carrying out PMIRRAS experiments is sketched in Fig. S6. For a complete description of the single pieces of equipment we used, see the Experimental Methods section in the manuscript.

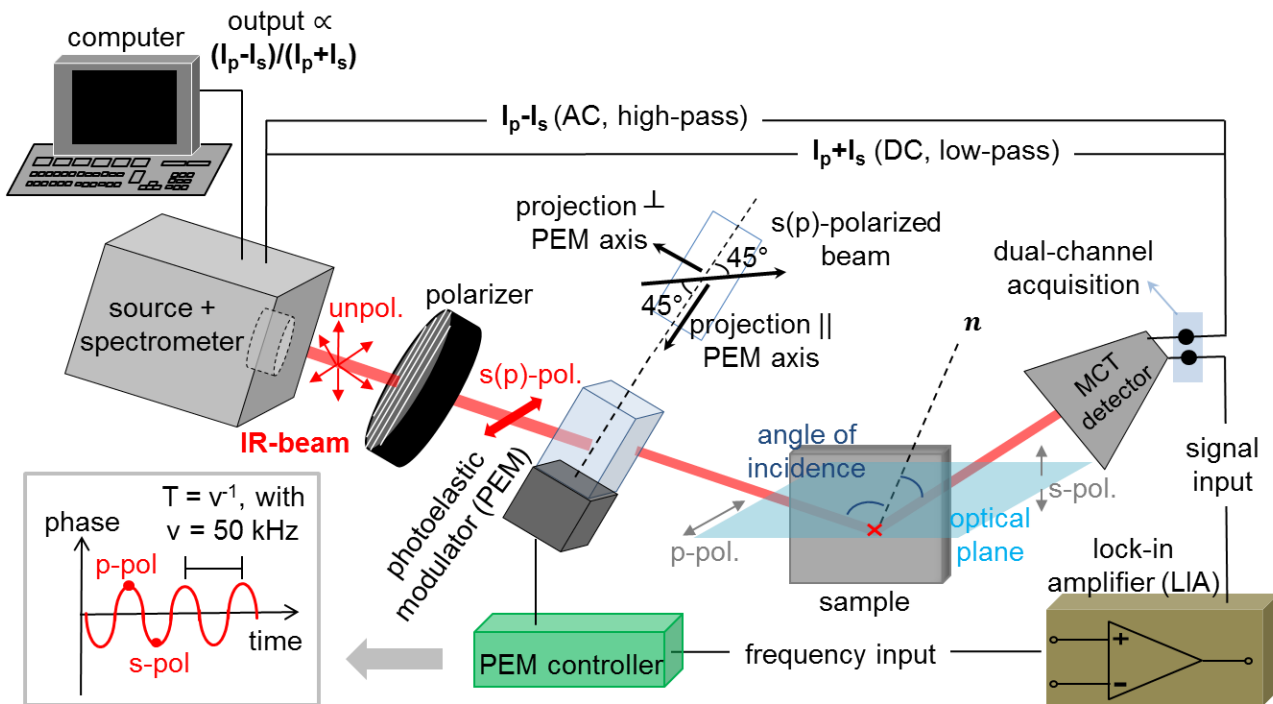


Figure S6: Sketch of typical setup for PMIRRAS experiments.

PMIRRAS data analysis

The raw PMIRRAS spectra (after Fourier transformation) are convoluted with the Bessel functions originating from the polarization modulation of the incident beam⁷. Such background needs to be removed for further analysis of the spectra. Usually, only the zeroth- and second-order Bessel functions, $J_0(\phi_0)$ and $J_2(\phi_0)$, contribute to the reflectivity signal⁸. However, using the software OPUS (Bruker) and following the procedure illustrated in the Bruker manual⁹ it is possible to remove the background arising from the polarization modulation by “pinning” specific points along the spectrum and fitting them to a polynomial of arbitrary degree. If a spectrum of the bare SiO_x/Au substrate is measured with the same modulation parameters, it provides a precise guideline for the fitting and subtraction procedure.

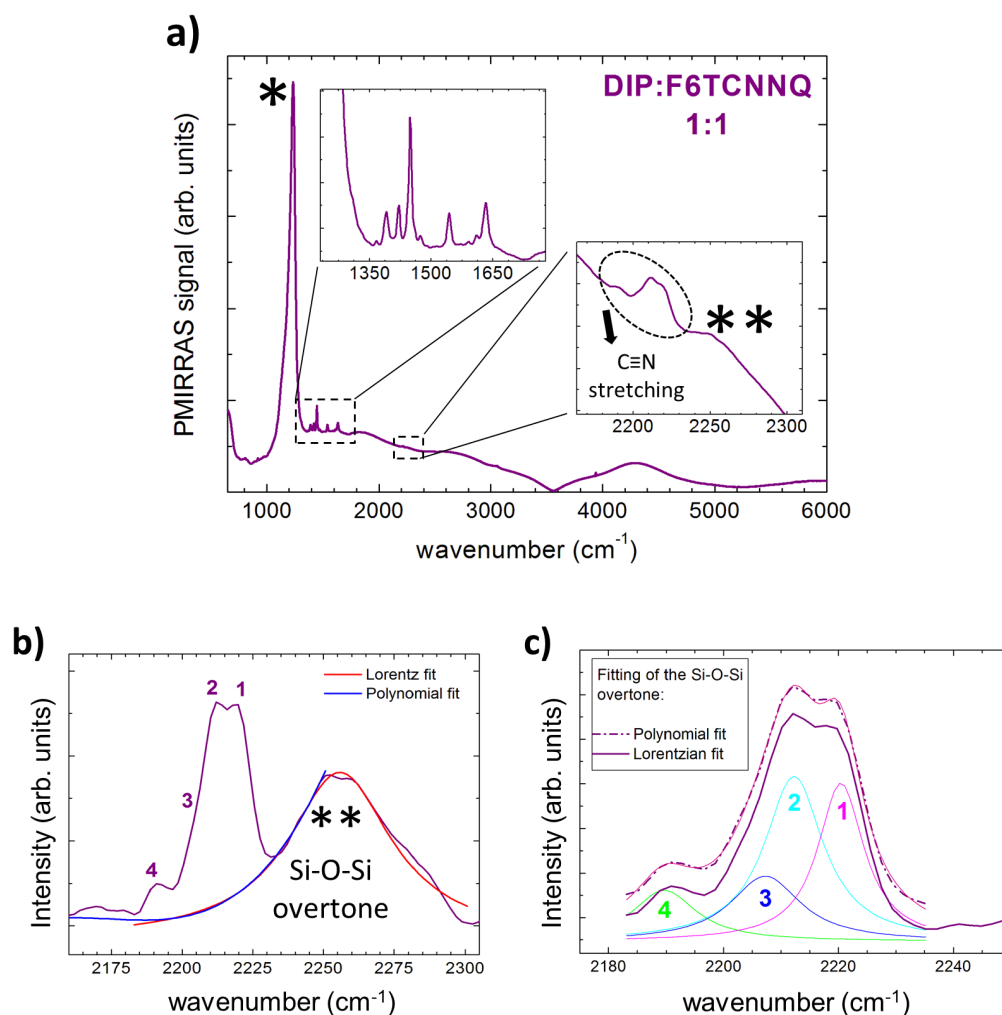


Figure S7: (a) Full-range raw PMIRRAS spectrum of the DIP:F₆TCNNQ 1:1 blend before subtraction of the Bessel background arising from the polarization modulation. The “*” on the strongest peak of the spectrum marks the asymmetric Si-O-Si stretching mode at $\sim 1235\text{ cm}^{-1}$. The first inset from the left shows a magnification of the C=C stretching region; the second inset shows a magnification of the C \equiv N stretching region, where “**” marks the overtone of the main Si-O-Si stretching peak. (b) Magnification of the C \equiv N stretching region after subtraction of the Bessel background, where the overtone of the Si-O-Si stretching has been marked. A simple Lorentzian function as well as a 5th-degree polynomial, respectively, were used to remove this broad peak. Note that with the Lorentzian function it is possible to fit the whole peak, while the polynomial only allows fitting of the low-energy edge which is overlapped with the molecular C \equiv N stretching modes. (c) Comparison of the two spectral profiles in the C \equiv N stretching region obtained after subtraction of the overtone band using the Lorentz and the polynomial fit, respectively. The two profiles show no difference for what concerns the relevant F₆TCNNQ peaks. Here the fit to the C \equiv N stretching vibrations and the corresponding numbering of the four Lorentzian peaks are also shown. The global fit is colored in pink and overlaps almost perfectly with the dash-dotted profile.

In Fig. S7a we show the peculiar shape of a PMIRRAS spectrum right after the operation of Fourier transformation. The very intense peak at $\sim 1235 \text{ cm}^{-1}$ dominating the spectrum (marked with “*”) stems from the transverse asymmetric Si-O-Si stretching of the SiO_x layer and is commonly observed in Si oxide-coated metal surfaces (see e.g. Ref. 3,8). The two inset magnifications show the region of the C=C and C \equiv N stretching, respectively. In the C \equiv N stretching region, the broad feature marked with “**”) represents an overtone of the Si-O-Si stretching peak at 1235 cm^{-1} . The overtone has been fitted using two different functions and then subtracted, as shown in Fig. S7b. Finally, in Fig. S7c the remaining C \equiv N stretching peaks have been fitted with a sum of Lorentzian curves in order to extract peak position. For these fits, a total number of 3 or 4 Bragg peaks has been assumed depending on the sample. Notice that with these fits no quantitative information can be extracted on peak intensity: however, peak position and qualitative information on relative peak strength are still accessible¹⁰.

Table S2: Summary of the fitted C \equiv N stretching peak positions. The letter “w” indicates that the corresponding peak has qualitatively rather low intensity.

sample	DIP	4:1	2:1	1:1	1:2	1:4	F ₆ TCNNQ	DIP on F ₆ TCNNQ
peak 1 (cm^{-1})	-	2220.0	2220.5	2220.4	2221.6	2222.4	2224.1	2223.8
peak 2 (cm^{-1})	-	2210.4	2212.7	2212.2	2214.5	2214.9	2215.5	2215.4
peak 3 (cm^{-1})	-	2201.6 w	2205.2 w	2207.3	2204.5	2204.7	2207.0	2204.0
peak 4 (cm^{-1})	-	-	2190.9	2189.7	2192.7	2195.0	-	-

In Tab. S2 we report the fitted peak positions for all DIP:F₆TCNNQ blends and the planar heterostructure. The corresponding statistical error bars associated with the fits can be inspected in Fig. 4b of the manuscript.

Details of the spectra in the C=C stretching region

Fig. 3 of the manuscript shows PMIRRAS spectra of DIP:F₆TCNNQ blends and pristine compounds. There, we discussed the red-shift of the strongest modes of F₆TCNNQ, suggesting its origin to be in the ground-state CT interactions between the donor DIP and the

acceptor F₆TCNNQ. We also discussed the presence of phase-separated F₆TCNNQ domains in each bulk heterojunction, even those with molar excess of DIP. To support this last point, we show in Fig. S8a,b the presence of a high-energy shoulder of given red-shifted F₆TCNNQ modes in the bulk heterojunctions.

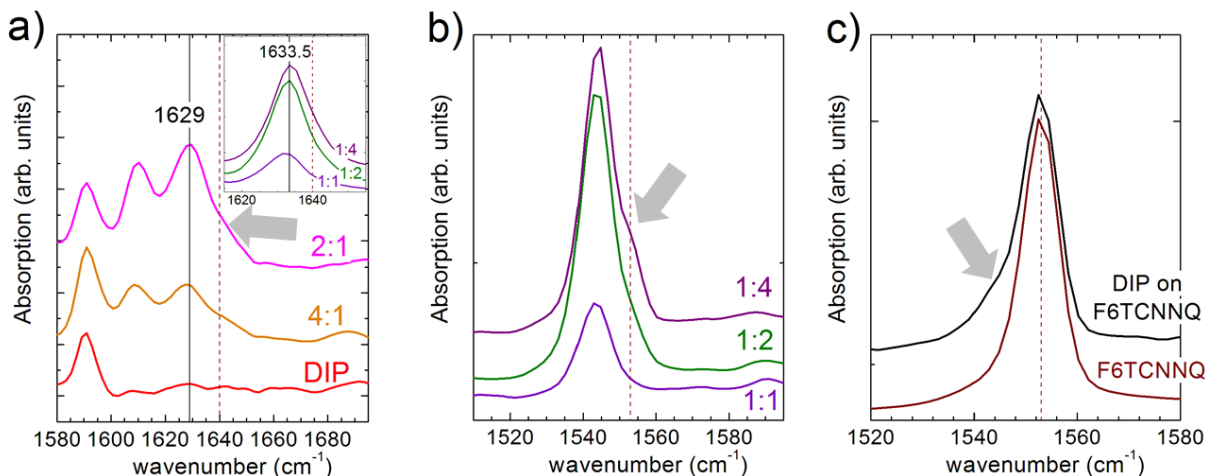


Figure S8: Magnifications of selected F₆TCNNQ resonance modes. The spectral portions are adapted from the spectra of Fig. 3 in the manuscript. The arrows indicate shoulders of the strongest peaks. The vertical dashed lines are in correspondence of the most intense peaks in the pristine F₆TCNNQ film, namely at 1640 cm⁻¹ in (a) and 1553 cm⁻¹ in (b) and (c). In (a), the vertical continuous line in the main panel is located at 1629 cm⁻¹, whereas in the inset it is located at 1633.5 cm⁻¹, and it evidences the further red-shift of the CT-affected peak when going from blends with excess F₆TCNNQ to blends with excess DIP.

Additionally, from inspection of the X-ray scattering data of the planar heterojunction (Fig. 2h of the manuscript) we concluded the presence of a relatively small amount of D:A co-crystal at the interface between the F₆TCNNQ islands and the DIP atop. This is confirmed by the presence of a low-energy shoulder of the strongest F₆TCNNQ modes in this film, an example of which is shown in Fig. S8c.

Comparing the inset of Fig. S8a with its main panel it is possible to identify a red shift by roughly 4.5 cm⁻¹ of the CT-affected F₆TCNNQ peak. We recall that such peak is already shifted towards lower energies in the bulk heterojunctions compared to pristine F₆TCNNQ as a result of CT interactions. The additional red shift when going from blends

with excess F_6TCNNQ to blends with excess DIP closely matches the observations in the $C\equiv N$ stretching region (see manuscript) and confirms that the local molecular environment affects peak position similarly to a solvent-shift.

In Fig. 3 of the manuscript, the two peaks marked with red squares have been assigned to pristine DIP, whose orientation with respect to the substrate surface changes in the mixtures with F_6TCNNQ . This orientation-transition results as a consequence of: a) nucleation of DIP crystallites in a more lying-down orientation (λ -orientation), b) inclusion of DIP molecules in the DIP: F_6TCNNQ co-crystal. In Fig. S9 we prove this by comparing the PMIRRAS spectrum of a DIP film in σ -orientation with a film in which DIP has been “artificially” produced having a λ -orientation according a procedure detailed elsewhere¹¹.

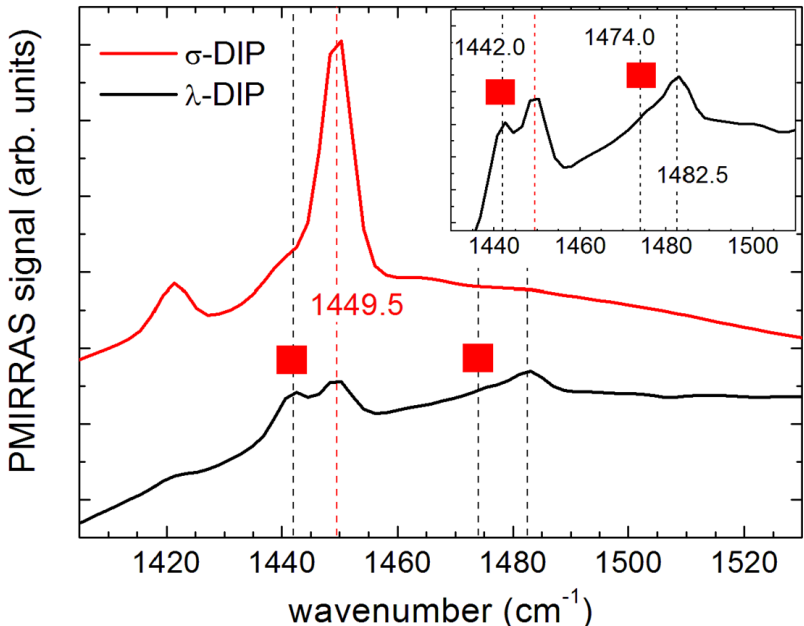


Figure S9: Raw PMIRRAS spectra of two films of pristine DIP in standing-up (σ) and lying-down (λ) orientation, respectively, on SiO_x layers on Au substrates. The DIP film in λ -orientation has been produced using a procedure detailed elsewhere¹¹. The vertical dashed lines mark the position of relevant peaks discussed in the manuscript. In particular, the red line marks the strongest DIP mode as in Fig. 3 of the manuscript. The red squares indicate the same two peaks as in Fig. 3 of the manuscript.

The red squares in Fig. S9 mark the same features as in Fig. 3 of the manuscript. In σ -DIP, the peak at 1442.0 cm^{-1} is just a shoulder of the strongest peak at 1449.5 cm^{-1} ,

whereas in λ -DIP the relative intensity of the two peaks is comparable. Our DFT calculations reproduce very well the experimental IR spectrum of pristine DIP (Fig. S10), in particular they correctly predict the strongest mode. However, no low-energy shoulder is expected by the calculations. We therefore assign the shoulder at 1442.0 cm^{-1} to a Davydov splitting of the peak at 1449.5 cm^{-1} . The relative intensity of the two Davydov components changes pronouncedly when going from the pristine DIP film to the mixtures due to re-orientation of DIP in both pristine crystallites and co-crystallites, as discussed in the manuscript. The presence of Davydov splitting also in the co-crystallites denotes pronounced inter-molecular interactions.

DFT also predicts the presence of the two peaks at 1474.0 and 1482.5 cm^{-1} for isolated DIP (Fig. S10, inset). In the λ -oriented DIP sample of Fig. S9 their relative intensity is inverted compared to what observed for the DIP:F₆TCNNQ mixtures in Fig. 3 of the manuscript. The relative intensity of these two peaks might be affected by the finer details of the molecular orientation and by the presence of DIP:F₆TCNNQ co-crystals with consequent CT interactions in the mixture. However, clearly the increase of the strength of these two features relative to the others is related to the orientational transition of the DIP molecules, i.e. they are *not* new features emerging as a consequence of D:A interactions.

DFT calculation of infrared spectra for isolated molecules

In Fig. S10 we show DFT calculations of the vibrational modes for the neutral form of isolated DIP. In Fig. S11 the same calculations for the neutral F₆TCNNQ molecule and for the F₆TCNNQ anion, respectively, are shown. The B3LYP functional was used with the 631Gd basis set. The wavenumber axis of the vibrational spectra was scaled by the factor 0.97^{12} .

For neutral F₆TCNNQ, the type of vibrations that constitute the strongest modes experimentally observed in the C=C stretching region are described in the calculated spectra

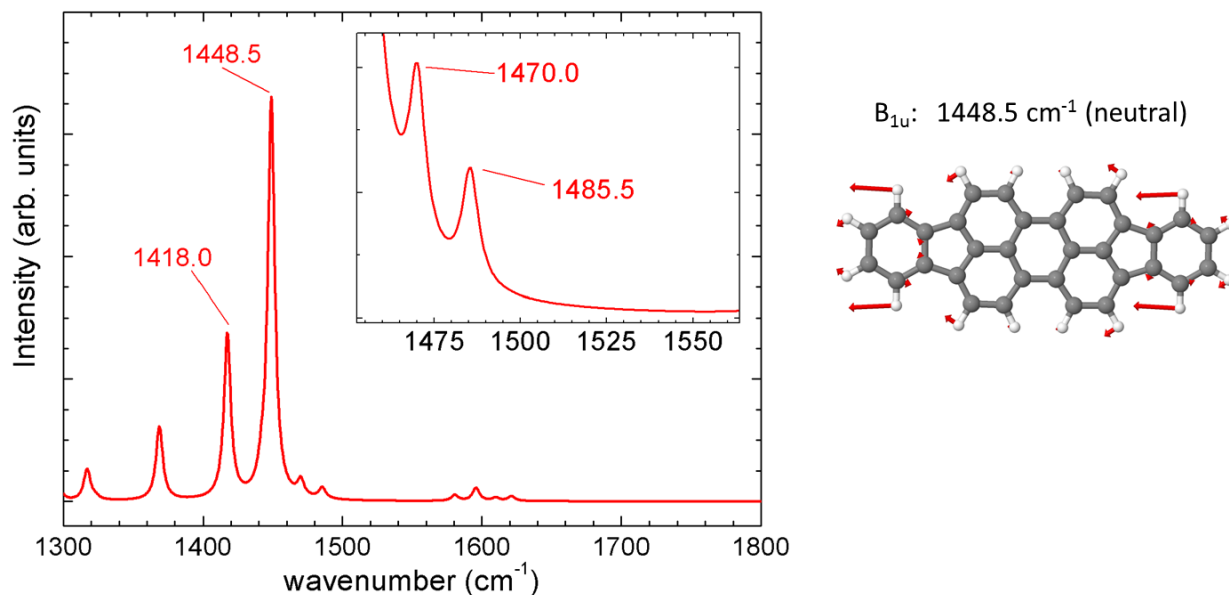


Figure S10: DFT simulation of IR-active molecular vibrations for isolated DIP in the neutral state. [LEFT] Simulated IR spectra in the range 1300-2260 cm^{-1} . The inset shows a magnification of the two peaks on the high-energy side of the most intense one. Rescaling of the abscissa due to anharmonicity of the molecular potential has been performed using the factor 0.97. [RIGHT] Illustration and energy position of the strongest IR-active mode for the neutral molecule.

of Fig. S11. For the $F_6\text{TCNNQ}$ mono-anion, the type of vibrations constituting the mode at $\sim 1615 \text{ cm}^{-1}$ are nearly identical to those constituting the mode at $\sim 1633 \text{ cm}^{-1}$ for the neutral molecule. This mode is therefore red-shifted by $\sim 18 \text{ cm}^{-1}$ when going from the neutral to the mono-ionized state. All other modes calculated in the $\text{C}=\text{C}$ stretching region for the mono-anion mostly do not retain the same type of vibrations found for the neutral molecule. In particular, the strongest mode located at $\sim 1400 \text{ cm}^{-1}$ in the mono-anion exhibits pronounced stretching of the hexoskeletal $\text{C}=\text{C}$ bonds and pronounced deformation of the benzenoid rings.

For the $\text{C}\equiv\text{N}$ stretching range, the high energy peak shifts by 33.0 cm^{-1} , whereas the low energy peak shifts by 43.5 cm^{-1} . It is quite likely that only the stronger B_u mode of the anionic $F_6\text{TCNNQ}$ calculated by DFT (right side of Fig. S11) can be detected experimentally in a meaningful way, which therefore represents our assignment of the observed peak 4 in

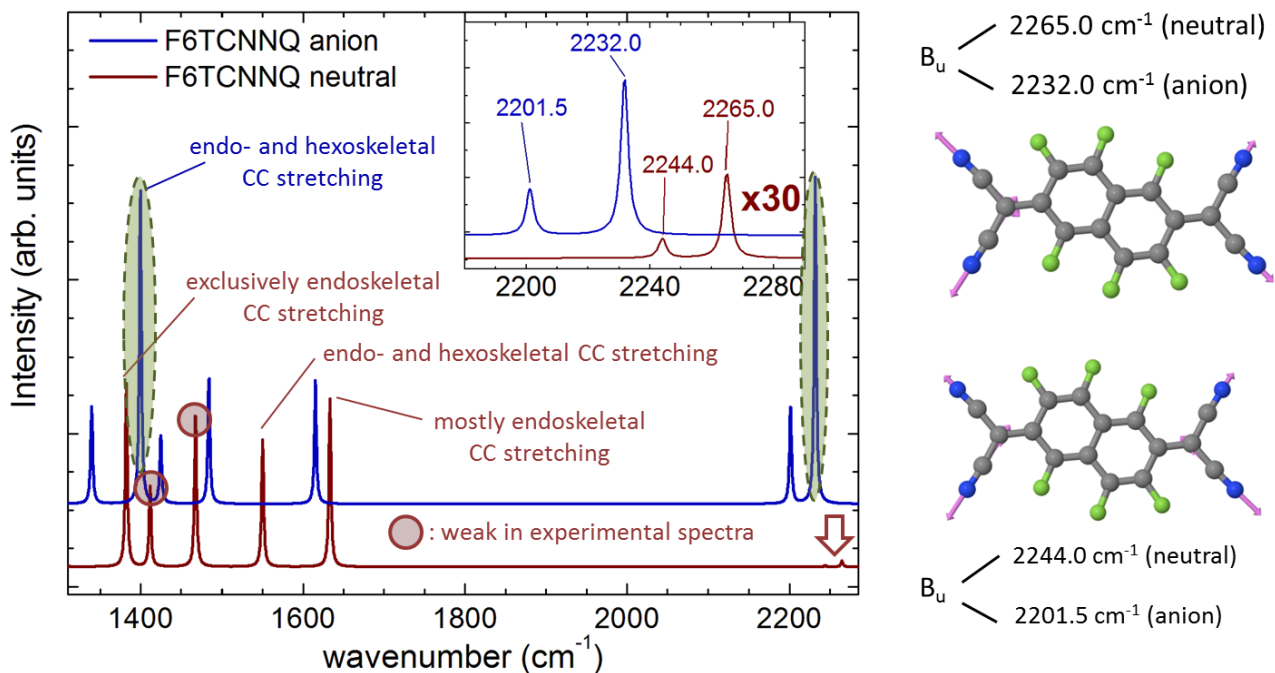


Figure S11: DFT simulation of IR-active molecular vibrations for isolated F_6TCNNQ in both the neutral state and the mono-anion. [LEFT] Simulated IR spectra in the range 1300-2275 cm^{-1} . The inset shows a magnification of the $C\equiv N$ stretching region, where the peaks of the neutral molecule multiplied by 30 in order to render them comparable with those of the mono-anion, which are red-shifted due to the quinoid-to-benzenoid transition upon ionization. For the mono-anion spectrum, the two strongest features have been circled in green as in Fig. 6 of the manuscript. The arrow points to the tiny $C\equiv N$ stretching modes for pristine F_6TCNNQ . Rescaling of the abscissa due to anharmonicity of the molecular potential has been performed using the factor 0.97. [RIGHT] Illustration and energy position of the two IR-active asymmetric $C\equiv N$ stretching modes for the neutral molecule and the mono-anion.

Fig. 4a of the manuscript.

The average red shift exhibited by the experimental CT peak with its systematic uncertainty is $27.7 \pm 1.3 \text{ cm}^{-1}$ (see manuscript). We calculate the average degree of CT, ρ_{avg} , using the empirical linear relationship suggested in Ref. 13 and taking the red-shift obtained from the DFT calculation for the F_6TCNNQ mono-anion as reference for case of integer CT. The stronger B_u mode exhibits a red-shift of 32.5 cm^{-1} from the neutral to the fully charged situation, which gives the degree of CT for F_6TCNNQ $\rho_{avg} = 0.85 \pm 0.04 \text{ cm}^{-1}$.

DFT calculations on single molecule can accurately reproduce the relative intensity of

IR-active modes¹⁴. Apart from the well-known red-shift of the resonance peaks due to the quinoid-to-benzenoid transition which accompanies the ionization process, another important difference between the calculated spectra of the neutral molecule and the mono-anion is the intensity of the C≡N stretching peaks relative to the peaks in the C=C stretching region, namely the relative strength of the C≡N stretching peaks is much higher for the mono-anion. In particular, in the mono-anion the oscillator strength of the strongest mode at $\sim 1400.0 \text{ cm}^{-1}$ in the C=C stretching region is very similar to the highest energy C≡N stretching mode at $\sim 2232.0 \text{ cm}^{-1}$.

The reason for this behavior is the pronounced increase in the net charge on the C≡N wings for the anion compared with the neutral molecule, which renders the transition dipole moment for the IR-allowed C≡N stretching modes much stronger and therefore increases their oscillator strength. The increase in net charge delocalized on the molecular backbone is not as strong due to the electron-withdrawing effect of the fluorine atoms. As a result, the oscillator strength of the C=C stretching modes does not increase as much as for the C≡N bonds. Therefore, inspection of the relative intensity of the resonances in the C≡N and C=C stretching range of experimental IR spectra can give qualitative information to discriminate between the two border-cases of full and no ionization, respectively.

Comparison of F₆TCNNQ powder and thin film

Fig. S12a shows a transmission spectrum of F₆TCNNQ powder in the C≡N stretching region, which is compared to the transmission spectrum of a pristine F₆TCNNQ film on native Si oxide and to PMIRRAS spectra of a pristine F₆TCNNQ film and of the DIP:F₆TCNNQ 4:1 mixture shown in Fig. 4a of the manuscript, respectively. From Fig. S12a it is clear that peak 1 and 2 are two distinct modes with a separation of $\sim 12.5 \text{ cm}^{-1}$, whereas peaks 2 and 3 are the Davydov components of the lower-energy mode with a split of $\sim 8.5 \text{ cm}^{-1}$. For pristine F₆TCNNQ films, the scenario is quite different (see manuscript). There, peak 1 and 2 are

the Davydov components of the high-energy $C\equiv N$ stretching mode, whereas peak 3 is the high-energy mode. This difference between thin film and powder can be attributed to the presence two different crystal polymorphs for the bulk and the film, respectively, as evidenced by X-ray diffraction (Fig. S12b). This comparison with F_6TCNNQ powder shows that it is important to correctly identify possible peak splittings due to solid-state interactions.

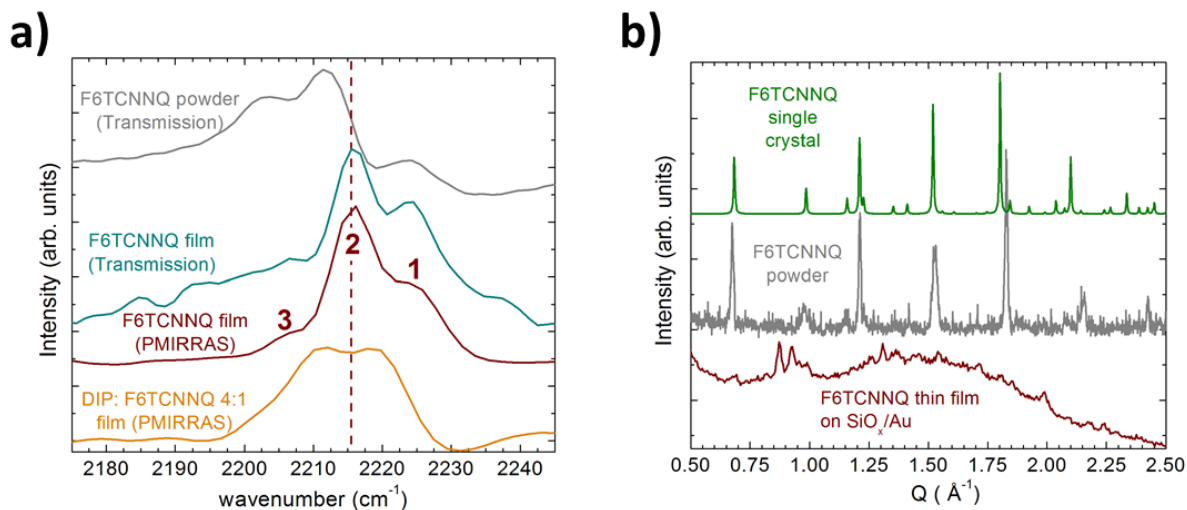


Figure S12: a) FTIR spectra of different F_6TCNNQ samples measured in different geometries. Grey trace: transmission spectrum obtained by sandwiching and sealing a dispersion of F_6TCNNQ powder in paraffin oil between two CaF_2 windows. Light green trace: transmission spectrum of a pristine F_6TCNNQ film on native Si oxide. Brown trace: PMIRRAS spectrum of a pristine F_6TCNNQ thin film on the SiO_x/Au substrate, same as shown in Fig. 4a of the manuscript. Orange trace: PMIRRAS spectrum of the 4:1 DIP: F_6TCNNQ blend, same as shown in Fig. 4a of the manuscript. The vertical dashed line marks 2215.5 cm^{-1} . b) Comparison of simulated X-ray diffraction scans of F_6TCNNQ single crystal (green trace, from Ref. 15) and experimental diffraction patterns for powder (gray) and thin film (brown), respectively. The slight mismatch between simulated single-crystal and experimental powder spectra at high Q -values is probably due to wrong atomic positions contained in the crystal structure file. The thin-film diffraction pattern was recorded in grazing-incidence geometry with closed slits between sample and detector in order to improve the signal-to-noise.

As seen in Fig. S12b, the F_6TCNNQ powder is strongly crystalline and it exhibits in FTIR three resonances for the $C\equiv N$ stretching. We note that our FTIR spectrum of F_6TCNNQ powder in this range is very similar to the spectrum presented in Ref. 16 as representative

of F₆TCNNQ.

Fig. S12b also shows a GIXD scan of the pristine F₆TCNNQ film measured using quite closed slits between the sample and the detector in order to improve the signal-to-noise and be able to measure clear Bragg peaks from this weakly crystalline material. A number of weak Bragg peaks and many other smaller features can be recognized. This proves the partially crystalline nature of this sample, but the crystallites lack long-range order. Due to the weakness of the diffraction peaks, it is likely that a good portion of the sample is completely amorphous. The remarkable difference between the diffraction pattern of thin film and powder/ single crystal points towards the presence of two (or possibly more) different F₆TCNNQ polymorphs for the thin film and the bulk material, respectively. Overall, it seems quite evident that the powder sample exhibits a much higher crystalline portion than the thin film.

The assignment of peaks 1-3 is different for the thin film and for the powder, respectively. In the thin film, peaks 1,2 are assigned to Davydov splitting of the strongest C≡N stretching mode having B_u symmetry, whereas peak 3 is the weaker, unsplit mode, which gets very broad and nearly vanishes in the DIP:F₆TCNNQ 4:1 mixture. In the powder, the low-energy peaks 2 and 3 are split by $\sim 8.5 \text{ cm}^{-1}$ and are assigned to the Davydov components of the low-energy mode. Peak 1 is $\sim 12.5 \text{ cm}^{-1}$ apart from the average position of peaks 2-3 and is therefore the high-energy C≡N stretching mode.

The difference seems to rely primarily on the presence of two crystal polymorphs for the powder and the thin film, respectively, as it is obvious from the X-ray diffraction data of Fig. S12. The crystalline packing of the F₆TCNNQ co-crystal¹⁵ might induce mode mixing compared to the mode energy ordering calculated by DFT for the isolated molecule, therefore accurate calculations would be required to assign the vibrations observed in the powder sample, which is obviously beyond the scope of this work.

References

- (1) Nečas, D.; Klapetek, P. Gwyddion: an open-source software for SPM data analysis. *Cent. Eur. J. Phys.* **2012**, *10*, 181–188.
- (2) Woollam, J. A. Guide to Using WVASE.. Spectroscopic Ellipsometry Data Acquisition and Analysis Software. *J. A. Woollam Co., Inc.* **2012**,
- (3) Zawisza, I.; Wittstock, G.; Boukherroub, R.; Szunerits, S. PMIRRAS Investigation of Thin Silica Films Deposited on Gold. Part 1. Theory and Proof of Concept. *Langmuir* **2007**, *23*, 9303–9309.
- (4) Dürr, A. C.; Schreiber, F.; Ritley, K. A.; Kruppa, V.; Krug, J.; Dosch, H.; Struth, B. Rapid Roughening in Thin Film Growth of an Organic Semiconductor (Diindenoperylene). *Phys. Rev. Lett.* **2003**, *90*, 016104.
- (5) Duva, G.; Pithan, L.; Zeiser, C.; Reisz, B.; Dieterle, J.; Hofferberth, B.; Beyer, P.; Bogula, L.; Opitz, A.; Kowarik, S. et al. Thin-Film Texture and Optical Properties of Donor/Acceptor Complexes. Diindenoperylene/F6TCNNQ vs Alpha-Sexithiophene/F6TCNNQ. *J. Phys. Chem. C* **2018**, *122*, 18705–18714.
- (6) ter Horst, J. H.; Cains, P. W. Co-Crystal Polymorphs from a Solvent-Mediated Transformation. *Cryst. Growth Des.* **2008**, *8*, 2537–2542.
- (7) Hipps, K. W.; Crosby, G. A. Applications of the photoelastic modulator to polarization spectroscopy. *J. Phys. Chem.* **1979**, *83*, 555–562.
- (8) Dunlop, I. E.; Zorn, S.; Richter, G.; Srotc, V.; Kelsch, M.; van Aken, P. A.; Skoda, M.; Gerlach, A.; Spatz, J. P.; Schreiber, F. Titanium-silicon oxide film structures for polarization-modulated infrared reflection absorption spectroscopy. *Thin Solid Films* **2009**, *517*, 2048–2054.
- (9) Bruker, PMA 50 user's manual. 2013.

- (10) Meier, R. J. On art and science in curve-fitting vibrational spectra. *Vib. Spectrosc.* **2005**, *39*, 266–269.
- (11) Duva, G.; Mann, A.; Pithan, L.; Beyer, P.; Hagenlocher, J.; Gerlach, A.; Hinderhofer, A.; Schreiber, F. Template-Free Orientation Selection of Rod-Like Molecular Semiconductors in Polycrystalline Films. *J. Phys. Chem. Lett.* **2019**, *10*, 1031–1036.
- (12) NIST, Vibrational scaling factors. <https://cccbdb.nist.gov/vibscalejust.asp>.
- (13) Chappell, J. S.; Bloch, A. N.; Bryden, W. A.; Maxfield, M.; Poehler, T. O.; Cowan, D. O. Degree of charge transfer in organic conductors by infrared absorption spectroscopy. *J. Am. Chem. Soc.* **1981**, *103*, 2442–2443.
- (14) Anger, F.; Scholz, R.; Gerlach, A.; Schreiber, F. Vibrational modes and changing molecular conformation of perfluororubrene in thin films and solution. *J. Chem. Phys.* **2015**, *142*, 224703.
- (15) Li, J.; Duchemin, I.; Roscioni, O. M.; Friederich, P.; Anderson, M.; Da Como, E.; Kociok-Köhn, G.; Wenzel, W.; Zannoni, C.; Beljonne, D. et al. Host dependence of the electron affinity of molecular dopants. *Mater. Horiz.* **2018**, *6*, 107–114.
- (16) Karpov, Y.; Erdmann, T.; Stamm, M.; Lappan, U.; Guskova, O.; Malanin, M.; Raguzin, I.; Beryozkina, T.; Bakulev, V.; Günther, F. et al. Molecular Doping of a High Mobility Diketopyrrolopyrrole-Dithienylthieno[3,2-b]thiophene Donor-Acceptor Copolymer with F6TCNNQ. *Macromolecules* **2017**, *50*, 914–926.